ACS Catalysis

Research Article

pubs.acs.org/acscatalysis

Propagation of Olefin Metathesis to Propene on WO_3 Catalysts: A Mechanistic and Kinetic Study

Zhuo Cheng and Cynthia S. Lo*

Department of Energy, Environmental and Chemical Engineering, Washington University, Saint Louis, Missouri 63130, United States

Supporting Information

ABSTRACT: The production of propene ($H_2C{=}CH{-}CH_3$) has attracted widespread interest due to industrial demand, and an intriguing route involves the metathesis of ethene ($H_2C{=}CH_2$) and *trans*-2-butene ($H_3C{-}CH{=}CH{-}CH_3$). We recently investigated the initiation of olefin metathesis on tungsten trioxide (WO_3) catalysts, by showing that *trans*-2-butene more readily forms W-carbene active sites on the surface, compared to ethene. We now present our analysis of the propagation steps at these active sites. We have computed optimized structures and energetics of the reaction intermediates and products of propagation. We have also computed the rate constants for the elementary steps comprising the reaction mechanism. These results are used to elucidate a complete mechanistic description of the metathesis of ethene and *trans*-2-butene. We find that $W{=}CH_2$ sites are less active in the propagation process compared to $W{=}CHCH_3$. Furthermore, [2 + 2] cycloaddition of *trans*-2-butene to form the six-membered (oxa)metallacycle ring is the rate-determining step; the rate constant is more sensitive to temperature and the reaction becomes faster than (oxa)metallacycle decomposition when the temperature exceeds 750 K. By revealing the relationship between the WO_3 surface structure and catalytic activity for olefin metathesis at different temperatures, we aim to use this information to predictively guide the development of more active and selective catalysts for propene production.

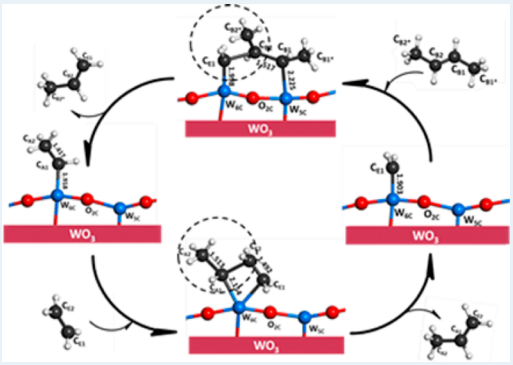

KEYWORDS: *DFT, tungsten oxide, metathesis, propagation, ethene, trans-2-butene, propene*

1. INTRODUCTION

Global demand for (poly)propene, which is an important building block for commodity chemicals ranging from plastic products to gasoline components, has spurred considerable attention on industrially viable routes to propene production. Compared to the traditional high temperature/pressure steam cracking method, olefin metathesis routes promoted by heterogeneous catalysts rely less on large sources of heat[1] and are carbon neutral. Generally, heterogeneous catalysts containing Re, Mo, or W[2−6] are favored over homogeneous catalysts for metathesis reactions due to their ease of separation, stability, and recyclability. Thus, olefin metathesis processes, which are solvent-free, generate little waste, and require low catalyst loads, are inherently energy-efficient and cost-effective;[7] however, concerns persist over the high temperatures and/or high pressures required to achieve high activity or selectivity.[8,9]

Catalyst materials based on transition metals, specifically Mo, Re, and W, are particularly promising due to the high reactivity of their unpaired d electrons, which can adopt multiple oxidation states to form active complexes and lower the energy barriers to metathesis reactions.[10] Handzlik investigated the metathesis activity of Mo methylidene species in zeolites and revealed that an $MoO(CH_2)$ (metal-carbene) fragment is a vital intermediate, with a high positive change, such that the oxygen site plays an important role in dictating the high catalytic activity.[11] Meanwhile, Luo et al. studied methyltrioxorhenium-catalyzed olefin cyclopropanation and found that the reaction is catalyzed by the metal Re site by forming a ReO structure.[12]

Tungsten trioxide WO_3 is well-known for its stability over industrial reaction temperature ranges, and it also can be easily deposited on supports using physical or chemical approaches.[4,13−15] Several researchers explored the use of alumina- or silica-supported WO_3 as a catalyst for metathesis between ethene and *trans*-2-butene. Chen et al.[16] found that the working lifetime of the WO_3 catalyst decreases with the w8 hly space velocity during metathesis reactions, which thus presents a useful guideline for engineering metathesis processes. Davazoglou et al.[17] obtained equal metathesis activity with well-dispersed, low loading WO_3/SiO_2 catalysts, compared to catalysts of higher tungsten content. Huang et al.[18,19] prepared a series of WO_3 catalysts by the thermal spread method and found that proportional correlation between the concentration of tetrahedral tungsten oxide species and catalytic activity for metathesis. While W is octahedrally coordinated in all solid WO_3 phases, such as the orthorhombic, monoclinic, and triclinic phases, it can assume a distorted octahedral coordination upon WO_3 deposition,[20] or even a tetrahedral coordination if the loading is small enough for W to interact

Received: April 21, 2014
Revised: November 5, 2014
Published: November 10, 2014

   dx.doi.org/10.1021/cs500531b | ACS Catal. 2015, 5, 59−72

directly with the support.[21] Liu et al.[22] deposited WO_3 on alumina supports and showed that a moist atmosphere hastened the calcination of the catalyst to expose surface facets. Chaemchuen et al. obtained Raman, UV−vis, and H_2-TPR spectra that suggest WO_3 catalysts calcined at 550 °C exhibit high activity for the metathesis of ethene and *trans*-2-butene to produce propene.[23] As the activity of the WO_3 catalyst appears to depend strongly on the calcination temperature during catalyst preparation, the catalysts calcined at 550 °C likely exhibit the orthorhombic phase.

Hérisson and Chauvin were the first to postulate that metathesis can proceed at modest temperatures through two processes: (1) initiation to form metal-carbene active sites; (2) propagation, including the [2 + 2] cycloaddition of (parallel-aligned) alkene double bonds to form metallocyclobutane intermediates at these metal-carbene active sites.[24−26] Szeto et al. investigated these two processes at low pressure and temperature using WH_3 active sites. Two parallel catalytic cycles have been proposed where the cycle involving the less sterically hindered tungstacyclobutane intermediates is most likely favored. It has been found that the arrangement of substituents on the least thermodynamically favored tungstacyclobutane governs the conversion rate of the cross metathesis reaction for propylene production from butenes and/or ethylene.[27] However, the two-step metathesis process has not still been fully understood, and the structure/activity relationships are not clear, due to limitations in experimentally detecting the molecular structure of metal-carbene active sites and metallocyclobutanes with current spectroscopic techniques.[28−31] First-principles calculations based on density functional theory can complement experimental mechanistic studies and provide valuable information on the structure of the active centers and the energy of adsorbates interacting with the surfaces.[32−36] In addition, detailed reaction pathways can be derived and characterized by the kinetic parameters of the constituent elementary steps.[37]

We recently performed a comprehensive density functional theory study of metathesis initiation on the orthorhombic WO_3 (001) surface.[38] Although W is octahedrally coordinated in this phase and not tetrahedrally coordinated as it would be for supported WO_3 clusters, it does appear to adopt a slightly distorted octahedral coordination in this surface plane so that W should be active for olefin metathesis. The (001) surface was chosen because our ab initio thermodynamics analysis indicated that the energy of formation of the (001) surface is an order of magnitude more favorable than those for the (100), (111), and (110) surfaces, respectively. The WO_3 crystal is easily cleaved along the (001) surface, because it is layered along this direction as a result of the antiferroelectric distortion of the W sublattice. Thus, good-quality single crystals of WO_3 (001) can be prepared by moderate heating in an oxygen-rich atmosphere and characterized using scanning tunneling microscopy (STM), low energy electron diffraction (LEED), and photoelectron spectroscopy (UPS, XPS).[39,40] We note that the highest energy barrier for metathesis using WO_3 is slightly higher than that using a Mo methylidene catalyst and similar to the barrier using a rhenium alkylidene oxo complex catalyst.[11,35,36,41] However, compared to the WO_3 structure, these metal alkylidene oxo systems may be unstable, because they are more easily affected by bimolecular decomposition, which is facilitated by a decrease in steric protection.[42] Finally, because WO_3 is potentially redox active[43,44] and the alumina and silica supports are relatively inert, any catalytic activity for olefin metathesis should arise from W. Thus, the use of a surface slab model gives a quantitative baseline of metathesis activity, from which more detailed analyses of catalyst surface structure and morphology—especially the coordination of W in anchored tungsten-carbene active sites—can be performed in the future for comparison.

Using this methodology, we showed that tungsten-carbene active sites readily form on the WO_3 (001) surface, so that metathesis between ethene and *trans*-2-butene[23] should be feasible. We revealed that the reaction pathways for W-carbene active site formation differs between ethene and *trans*-2-butene, though both proceed via five-step processes. In the ethene pathway, six-membered, five-membered, and four-membered (oxa)metallacycles are formed successively. However, in the *trans*-2-butene pathway, only five-membered and four-membered (oxa)metallacycles are formed. We also found that the opening of the four-membered (oxa)metallacycle is the rate-limiting step of the ethene pathway, while the forming of the five-membered (oxa)metallacycle is the rate-limiting step of the *trans*-2-butene pathway. We ultimately found that *trans*-2-butene preferentially forms W-carbene active sites, compared to ethene, due to the presence of electrophilic and steric effects that destabilize the intermediates.

In this work, we studied metathesis propagation on the WO_3 (001) surface, as cleaved from the orthorhombic bulk; this allowed for consistency with our previous study.[38] We first calculated detailed geometries and energetics of reaction intermediates and products. Next, we modeled various configurations for adsorbed ethene and adsorbed *trans*-2-butene, and we compared the thermodynamic stability of the resulting (oxa)metallacycle species. We then studied the pathways of propagation proceeding on the stable W-carbene species and determined the rate-limiting step. We also developed a thorough kinetic model of the metathesis reaction over the WO_3 (001) surface, based on transition-state theory. Such a technique, which explicitly takes into account the entropic contributions, allowed us to calculate rate constants for elementary steps and quantify their responses to changes in temperature. These results will hopefully guide the development of more active catalysts and more suitable reaction conditions for propene production.

2. METHODS

2.1. Structural Optimization. Tungsten trioxide (WO_3) exhibits a perovskite-like structure, with corner-sharing WO_6 octahedra.[45−47] However, structural analyses of WO_3 have revealed considerable deviations from the ideal cubic perovskite type, with the majority of these distortions corresponding to antiferroelectric displacements of W atoms and mutual rotations of oxygen octahedra.[48] In accordance with our previous study on metathesis initiation,[38] we used the orthorhombic phase for bulk WO_3; its space group is *Pmnb*, with a = 7.341 Å, b = 7.570 Å, and c = 7.754 Å.[49] The deviation from the ideal perovskite structure is characterized by a zigzag motion of the W atomic positions in the b and c directions, as well as a tilt relative to the a direction.[23,49,50]

The WO_3 bulk is easily cleaved along the (001) surface, because it is layered along this direction as a result of the antiferroelectric distortion of the W sublattice;[51,52] indeed, good quality single crystals of WO_3 (001) can be prepared by moderate heating in an oxygen-rich atmosphere[53−55] and characterized using scanning tunneling microscopy (STM), low energy electron diffraction (LEED), and photoelectron spec-

dx.doi.org/10.1021/cs500531b | ACS Catal. 2015, 5, 59−72

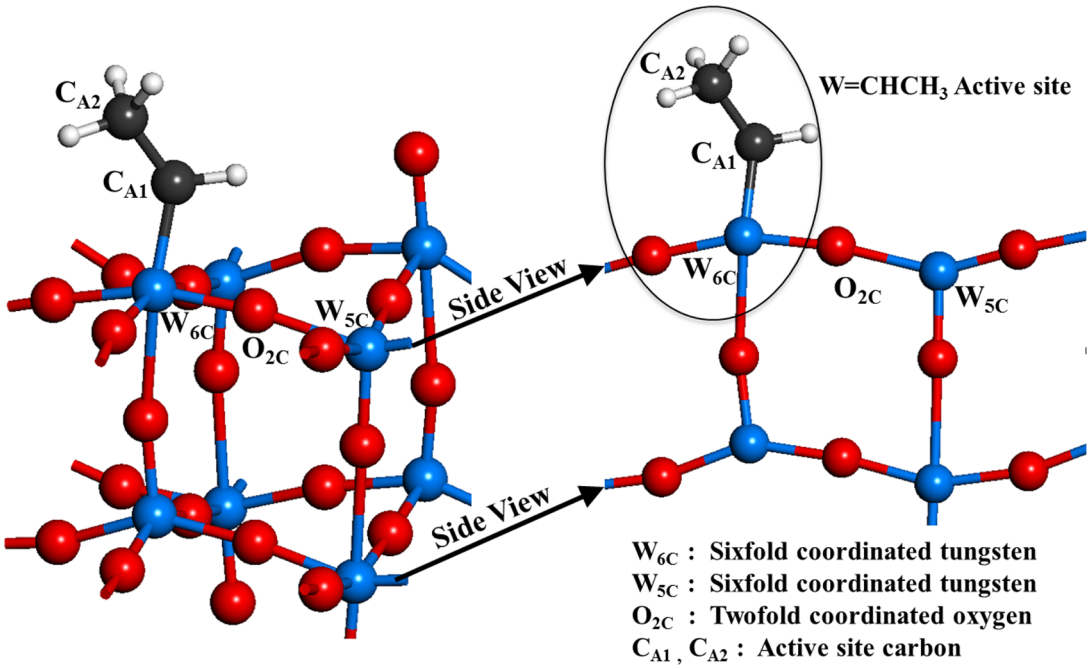

Figure 1. Geometry-optimized WO_3 (001) surface with W=CHCH$_3$ active site. Because of the repeated W_{6c}–O_{2c}–W_{5c} structural motif on the surface, we employ a side view to represent the supercell.

troscopy (UPS, XPS).[39,56] Thus, to build the surface slab models, the WO_3 bulk is cleaved along the (001) surface, which is also chosen for consistency with our previous study on active sites formation over WO_3.[38] We used a five-layer semi-infinite slab to model the WO_3 (001) catalyst structure with W=CH_2CH_3 active sites. The use of the periodic models avoids the introduction of edge effects and allows for a more accurate description of surface relaxation.

All calculations were performed within the framework of density functional theory (DFT), using the Vienna Ab Initio Simulation Package (VASP 5.2)[57−59] and the generalized gradient approximation of Perdew, Burke, and Ernzerhof[60] to represent the exchange-correlation energy. The Projector Augmented-Wave (PAW) method,[61,62] with a 400 eV energy cutoff, was used to describe the wave functions of the atomic cores. The tetrahedron method with Blöchl corrections[63] was used to set the partial occupancies for the orbitals. While a *k*-point mesh size of 6 × 6 × 1 was used for the WO_3 surface slab in our previous study,[38] we ultimately used the 3 × 3 × 1 Γ-centered Monkhorst−Pack *k*-point mesh for the WO_3 surface with W=CH_2CH_3 active sites, which still gave results that were sufficiently converged (within 1×10^{-5} eV using the conjugate gradient method). We observed that spin-polarized calculations did not yield significant changes to the calculated energies compared to nonspin-polarized calculations.[64]

We optimized the structure of active sites W=CH_2CH_3 to get a W=C bond length of 1.918 Å, and a C−C bond length of 1.496 Å. A $p(2 \times 2)$ supercell was used to ensure that all adsorbates do not interact with their periodic images (i.e., separation by at least 10 Å). The WO_3 (001) surface with W=CH_2CH_3 active sites thus consists of five chemically distinguishable types of surface atoms (Figure 1):

1. 5-fold coordinated tungsten W_{5c}
2. 6-fold coordinated tungsten W_{6c}
3. 2-fold bridging oxygen O_{2c}
4. Active-site carbon C_{A1} binding to surface W_{6c} atom
5. Active-site carbon C_{A2} from CH_3 group

2.2. Energetics of Activation and Reaction. The energy of adsorption, E_{ads}, for the olefin molecules on the surface is defined as

$$E_{ads} = E_{adsorbate+surface} - E_{surface} - E_{adsorbate}$$

where $E_{surface}$ is the total energy of the surface slab, $E_{adsorbate}$ is the total energy of the gas-phase adsorbate, and $E_{adsorbate+surface}$ is the total energy of the composite system. Because the calculations are performed at 0 K and fixed cell volume, the differences in Gibbs free energy should equal the differences in total energy. By this definition, a negative value of E_{ads} corresponds to an exothermic and spontaneous adsorption process.

For calculating energies of adsorption, the inclusion of an empirical dispersion correction[65] appeared to affect the total energies of all reactant and product species almost equally; for example, the energy of adsorption for ethene changed only from −20.7 kJ/mol to −23.8 kJ/mol upon addition of the dispersion correction, and no change in the preferred site for adsorption was noted. Thus, for comparing trends in energies of adsorption in this catalytic system, the uncorrected PBE functional should be sufficient, and again, would provide consistency with our previous study on metathesis initiation.[38]

We also assume that for surface-mediated reactions, the change in Gibbs free energy with temperature can be quantified as $((\partial G)/(\partial T))_P = -S$, which we can assume is primarily due to the vibrational component. We thus carried out a vibrational analysis in order to validate the optimized geometry of the adsorbed species and transition states. All W atoms were rigidly constrained during these calculations. The Hessian dynamical matrix was obtained by numerical differentiation of the forces and diagonalized, which provided the harmonic molecular frequencies and the normal modes. These calculations made it possible to compute zero-point energy (ZPE) corrected energies and vibrational partition functions.

dx.doi.org/10.1021/cs500531b | ACS Catal. 2015, 5, 59−72

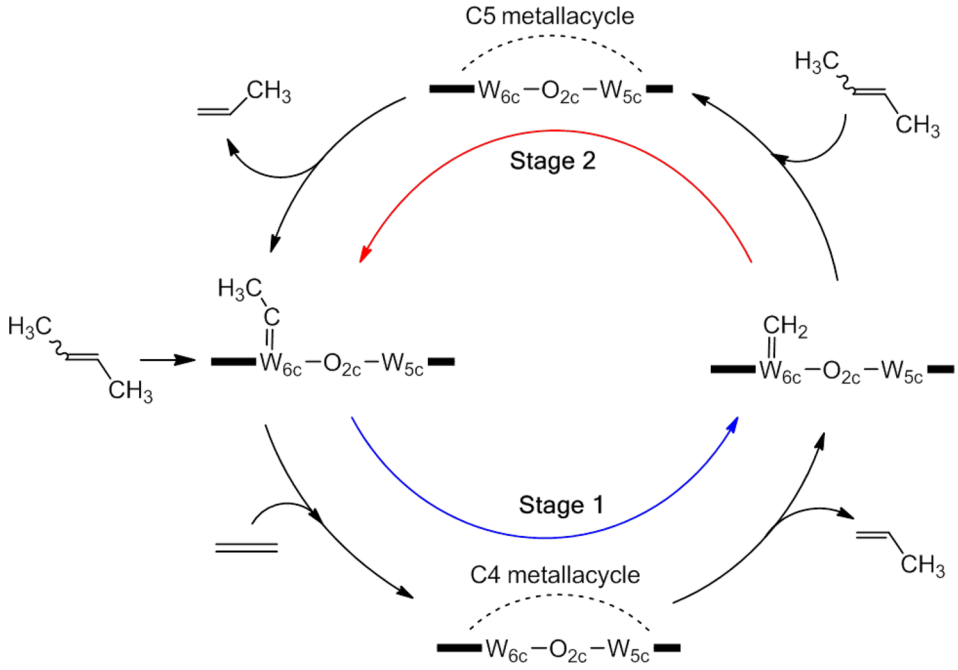

Figure 2. Proposed mechanism of metathesis propagation on $WO_3(001)$ catalysts, staring from $W{=}CHCH_3$ active site. Reactants, intermediates, and products are shown.

To locate transition states and calculate the energies of activation and resulting reaction pathways, we used the climbing-image nudged elastic band (CI-NEB) method,[66,67] with four images between the initial and final states. This method enabled us to map out stationary points along the minimum energy paths, and identify transition states, for each of the propagation process on WO_3 surface with W = carbene active sites. Because these paths were directed by force projection, the energy was not necessarily consistent with the force being optimized; thus, we chose the force-based quick-min optimizer to ensure the convergence of the nudged elastic band algorithm. The time step employed was 0.01 fs.

2.3. Kinetics of Reaction. The heat capacity, $C_p = T((\partial S)/(\partial T))_P$, was computed numerically, by differentiating the entropy that was previously computed from the vibrational partition function. Due to the lack of experimental data for S and C_p of the adsorbed species, we validated our methodology on gas phase ethene, and we found that the calculated entropy and C_p are in good agreement with the data from Yaw's handbook[68] (i.e., the maximum relative error is less than 5%). For adsorbed species, the vibrational entropy contribution can be obtained using the same methodology as the gas phase species, while assuming that the translational and rotational contributions are negligible and taking into account the relevant energies of adsorption and desorption when comparing to the gas phase values. With these assumption and modification in place, we are confident that this procedure should work well for adsorbed species, including (oxa)metallacycles, since the errors involved are negligible.

To obtain enthalpy, H, estimates at finite temperature, T, for all (oxa)metallacycle intermediates and products, the electronic energy was corrected for the zero point energy (ZPE) contribution and temperature variation (i.e., using C_p). Technically, $T = 0$ K results in an undefined value during the evaluation of C_p, as the temperature appears in the denominator. We can approximate $H(0\ \mathrm{K}) \approx H(1\ \mathrm{K})$, and define its value by $H(1\ \mathrm{K}) = U(0\ \mathrm{K}) + \mathrm{ZPE}$, where U is the total energy calculated from DFT.

Thus, the enthalpy can be obtained from eq 1 as below:

$$H(T) = U(0\mathrm{K}) + \mathrm{ZPE} + \int_1^T C_p(T')\mathrm{d}T' \tag{1}$$

Similarly, we can obtain the reaction enthalpy, ΔH_{rxn} for the forward and reverse elementary steps at finite temperatures.

Within the framework of a kinetic model, the activation energy can not be fitted independently, due to the thermodynamic constraint that ΔH_{rxn} equals the difference between the forward activation energy barrier, $E_{\mathrm{a,\ f}}$, and reverse activation energy barrier, $E_{\mathrm{a,\ r}}$. Hence, we develop a related eq 2 to calculate the activation energy for an elementary reaction:

$$E_{\mathrm{a,f}}(T) = E_{\mathrm{a,f,DFT}} + \beta(\Delta H_{\mathrm{rxn}}(T) - \Delta E_{\mathrm{rxn,\ DFT}}) \tag{2}$$

where $E_{\mathrm{a,\ f,\ DFT}}$ corresponds to the forward activation energy barrier and $E_{\mathrm{a,\ r,\ DFT}}$ corresponds to the reverse activation energy barrier at 0 K; they are constants obtained from DFT calculations.

The reaction enthalpy at finite temperature, $\Delta H_{\mathrm{rxn}}(T)$, is calculated from the enthalpies of the initial state and final state for the constituent elementary reactions. $\Delta E_{\mathrm{rxn,\ DFT}}$ is the difference between the energies of final state and initial state at 0 K, as derived from DFT and kept as constants throughout the calculations. The variable β denotes the relative position of the transition state compared to the initial (i.e., $\beta = 0$) or final (i.e., $\beta = 1$) state of the relevant elementary reaction. It can be obtained by considering which image in the CI-NEB calculations (out of four) corresponds to the transition state. When the value of β is close to 0, it describes to an initial-like transition state; thus, the forward activation energy may be kept at the DFT value, while the reverse activation energy is temperature dependent and needs to be thermodynamically calculated by analogy to eq 2. When the value of β is close to 1, it corresponds a final-like transition state; thus, the reverse

dx.doi.org/10.1021/cs500531b | ACS Catal. 2015, 5, 59−72

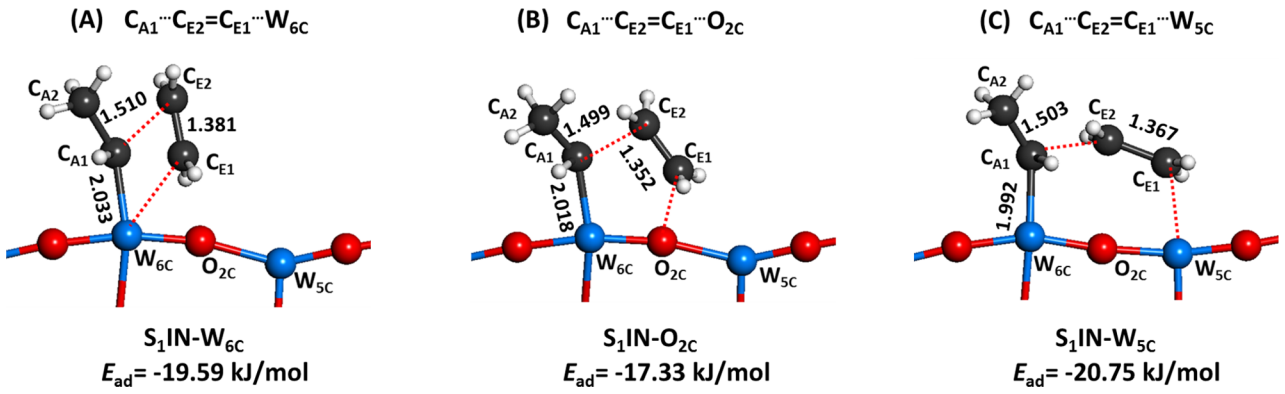

Figure 3. Adsorption configurations and energies for ethene on WO_3 (001) with W=$CHCH_3$ active site. C_{E1} and C_{E2} denote two carbon atoms in ethene. C_{A1} and C_{A2} denotes two carbon atoms in active site. S_1 denotes Stage 1 of the propagation process, and IN denotes the initial state for propagation.

activation energy may be kept at the DFT value, while the forward activation energy is corrected using eq 2. Otherwise, for intermediate values of β, the difference between $\Delta H_{rxn}(T) - \Delta E_{rxn,\,DFT}$ affects both the forward activation energy and reverse activation energy. This calculation technique is based on the Brønsted−Evans−Polanyi relationship, which states that the difference in activation energy between two reactions of the same family is proportional to the difference of their enthalpies of reaction.[69−71]

The energies of activation at the transition states are also corrected via ZPE and C_p. The pre-exponential factor, A, is calculated from the entropy differences between the initial and transition states of the respective elementary step, as shown below in eq 3:

$$A(T) = \left(\frac{k_B T}{h}\right)\left(\frac{Q_{TS}}{Q_0}\right) \tag{3}$$

where Q_{TS} and Q_0 are the partition functions of transition states and initial states, respectively. k_B is Boltzmann's constant, and h is Planck's constant. The partition functions themselves are approximated with the vibrational contribution being dominant.

The mathematical and thermodynamical calculations above enable us to obtain the relationship between reaction rate constants and temperature by the Arrhenius form in eq 4, using the calculated $E_{a,\,f}(T)$ and $A(T)$:

$$k(T) = A(T)\exp\left(-\frac{E_{a,f}(T)}{k_B T}\right) \tag{4}$$

Similarly, we can calculate the reverse rate constant by substituting instead $E_{a,\,r}(T)$.

3. RESULTS AND DISCUSSION

3.1. Proposed Mechanism for Propagation of Olefin Metathesis to Propene on W-Carbene Active Sites. During metathesis propagation, W=$CHCH_3$ first reacts with ethene to form propene and W=CH_2, which then further reacts with *trans*-2-butene to yield the second propene molecule. Our previous study on W-carbene active site formation showed that *trans*-2-butene preferentially reacts with 6-fold coordinated tungsten at the surface to form a W=$CHCH_3$ active site;[38] *trans*-2-butene is favored over ethene due to the presence of electrophilic and steric effects that destabilize the intermediates. Therefore, the W=$CHCH_3$ active site is the initial state of the propagation cycle, as shown in Figure 2.

Thus, we propose that the first stage of propagation is composed of ethene [2 + 2] cycloaddition at the W=$CHCH_3$ active site and cycloreversion of the first (oxa)metallacycle to form the first propene molecule, and the second stage is composed of *trans*-2-butene [2 + 2] cycloaddition at the W=CH_2 active site and cycloreversion of the second (oxa)-metallacycle to form the second propene molecule. The (oxa)metallacycle may be either the four-membered ring with W_{6c} and carbon; five-membered ring with W_{6c}, O_{1c}, and carbon; or six-membered ring with W_{6c}, W_{5c}, and carbon. In the following section, we present optimized (oxa)metallacycle structures for each stage of propagation, model propagation on WO_3 (001) catalysts, and we determine the rate-limiting step and investigate the thermal kinetics at each stage of the propagation cycle by calculating the rate constants of elementary steps.

3.2. Propagation of Ethene for Metathesis. *3.2.1. Ethene Adsorption on W=$CHCH_3$ Active Site.* As propagation is defined as the redistribution of fragments of alkenes by the scission and regeneration of carbon−carbon double bonds, the ethene molecule should bind to the W=$CHCH_3$ active site by [2 + 2] cycloaddition of two carbon−carbon double bonds. In our calculations, the free ethene is in gas phase, so we study ethene adsorption to the surface prior to the reaction. The adsorption of ethene molecules, with their C_{E1} and C_{E2} atoms, at the W=$CHCH_3$ active site can proceed by three types of two-site adsorption:

(A) C_{A1}···C_{E2}=C_{E1}···W_{6c}: C_{E1} and C_{E2} adsorb to 6-fold coordinated tungsten W_{6c} and active site carbon C_{A1}, respectively

(B) C_{A1}···C_{E2}=C_{E1}···O_{2c}: C_{E1} and C_{E2} adsorb to 2-fold coordinated oxygen O_{2c} and active site carbon C_{A1}, respectively

(C) C_{A1}···C_{E2}=C_{E1}···W_{5c}: C_{E1} adsorbs to 5-fold coordinated tungsten W_{5c}, while C_{E2} adsorbs to C_{A1}

S_1 denotes Stage 1 of the propagation process, and IN denotes the initial state for propagation.

After geometry optimization, the ethene molecule moves in space to find the most energetically stable adsorption structures and energies. The corresponding configurations are shown in Figure 3. For C_{A1}···C_{E2}=C_{E1}···W_{6c} adsorption, corresponding to (A)-type binding, the ethene molecule in vertical orientation tilts slightly relative to the orientation of W_{6c}−C_{A1}. It leads to a

dx.doi.org/10.1021/cs500531b | ACS Catal. 2015, 5, 59−72

four-membered ring, S_1IN-W_{6c}, which includes four active atoms, W_{6c}, C_{A1}, C_{E1}, and C_{E2}. For (B)-type binding, it produces a five-membered ring, S_1IN-O_{2c}, which includes five active atoms, W_{6c}, C_{A1}, C_{E1}, C_{E2}, and surface O_{2c}. For (C)-type binding $C_{A1}\cdots C_{E2}=C_{E1}\cdots W_{5c}$, the six-membered (oxa)-metallacycle ring S_1IN-W_{5c} is formed.

Figure 3 and Table 1 show that the (C)-type binding configuration is the most energetically favorable, with

Table 1. Calculated Energies of Adsorption for Ethene and *trans*-2-Butene Cycloaddition on WO_3 (001) with W-Carbene Active Sites

	two-site binding	
adsorption configuration	ethene E_{ads} (kJ/mol)	*trans*-2-butene E_{ads} (kJ/mol)
$C_{active\ site}\cdots C=C\cdots W_{6c}$	−19.6	−0.3
$C_{active\ site}\cdots C=C\cdots O_{2c}$	−17.3	−8.9
$C_{active\ site}\cdots C=C\cdots W_{5c}$	−20.8	−12.4
	one-site binding	
adsorption configuration	ethene E_{ads} (kJ/mol)	*trans*-2-butene E_{ads} (kJ/mol)
$W_{6c}\cdots C=C$	–	–
$W_{5c}\cdots C=C$	−17.3	−9.8
$O_{2c}\cdots C=C$	−4.3	−2.1
$C_{active\ site}\cdots C=C$	−7.2	−3.5

Table 2. Calculated Changes in Bond Lengths upon Ethene Adsorption at W-Carbene Active Sites and Formation and Cycloreversion of (Oxa)Metallacycles

adsorption	W=C (Å)	$C_{E1}-C_{E2}$ (Å)
before adsorption	1.918	1.339
(A): S_1IN-W_{6c}	2.033	1.381
(B): S_1IN-O_{2c}	2.018	1.352
(C): S_1IN-W_{5c}	1.992	1.367

formation	W=C (Å)	$C_{E1}-C_{E2}$ (Å)	W−C_{E1} or O−C_{E1} (Å)	$C_{A1}-C_{E2}$ (Å)
S_1IN-W_{6c}	2.154	1.492	2.013	1.896
S_1IN-O_{2c}	2.113	1.375	1.868	1.973
S_1IN-W_{5c}	2.089	1.489	2.245	1.822

cycloreversion	W=C (Å)
S_1IN-W_{6c}	1.924
S_1IN-O_{2c}	1.924
S_1IN-W_{5c}	1.924

corresponding bond lengths shown in Table 2. Both the $W_{6c}-C_{A1}$ and $C_{E1}-C_{E2}$ bonds in the (C)-type binding configuration are elongated compared to their values prior to adsorption; this suggests that the molecule is activated. The (A)-type binding configuration is slightly less energetically favorable, even though the W=C bond at the surface and the C=C bond in the ethene molecule are even longer than that in the other adsorption configurations. This may be attributed to the small four-membered ring inducing a stronger steric effect than the six-membered ring, such that the overlapping electron clouds result in elongation of the W=C bond in the (A)-type binding configuration to reduce the cost in energy. By comparing the area formed by the rings, using all obtained data on bond lengths, we can conclude that the location where there is less shielding reduces the net intermolecular forces acting on the ethene molecule; thus, the (C)-type binding configuration is relatively stable compared to the (A)-type binding configuration. By contrast, the (B)-type binding configuration to form a five-membered ring is the least energetically favorable. The ethene molecule is only slightly activated, and the low energy of adsorption may be attributed to the weak interaction between oxygen atoms in metal oxide and carbons atom in the alkene. This suggests that tungsten atoms are more active than oxygen atoms for small alkene propagation on the WO_3 (001) surface. For all configurations, the methyl group has not been affected upon adsorption and only moves slightly away (≈ 0.01−0.02 Å) from the carbon atom of the metal-carbene active site.

To ensure that we have a complete understanding of ethene behavior in the surface, we have also considered single-site adsorption of the molecule. All of the calculated adsorption energies are also shown in Table 1. We found the single-site absorption configurations are generally energetically unfavorable compared to the corresponding two-site adsorption configurations. As it does not appear that this pathway would be preferred for propagation, we will not discuss it further here, although they could be explored as the subject of future work on side reactions to the main Hérisson−Chauvin mechanism.

3.2.2. Formation and Cycloreversion of the C_4 (Oxa)-Metallacycle. Adsorbed ethene reacts with a $W=CHCH_3$ active site to form a C_4 (four carbon atoms in total) (oxa)metallacycle species by [2 + 2] cycloaddition. Based on three type of adsorption configurations, three possible C_4 (oxa)metallacycles can be obtained, as shown in Figure 4:

- (oxa)metallacycle species S_1IM-W_{6c} from ethene [2 + 2] cycloaddition on adsorption sites C_{A1} and W_{6c}
- (oxa)metallacycle species S_1IM-O_{2c} from ethene cycloaddition on adsorption sites C_{A1} and O_{2c}

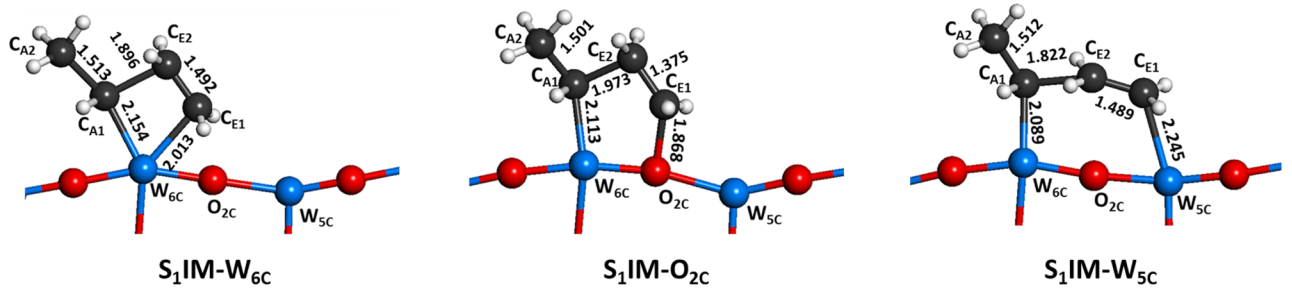

Figure 4. Optimized structures of (oxa)metallacycles from ethene [2 + 2] cycloaddition on WO_3 (001) with $W=CHCH_3$ active site. S_1 denotes Stage 1 of the propagation process, and IM denotes the intermediate.

dx.doi.org/10.1021/cs500531b | ACS Catal. 2015, 5, 59−72

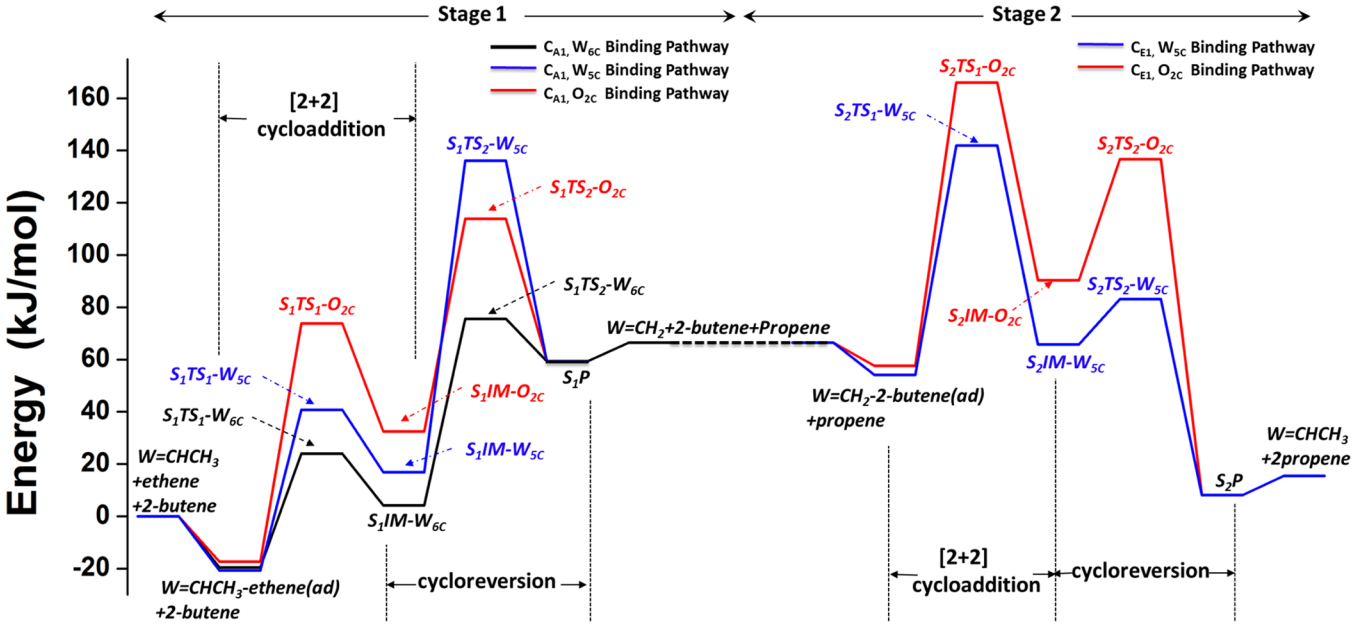

Figure 5. Minimum energy paths for ethene propagation at Stage 1 by binding to C_{A1} and W_{6c} (black), C_{A1} and O_{2c} (red), and C_{A1} and W_{5c} (blue); and for 2-butene propagation at Stage 2 by binding to C_{E1} and W_{5c} (blue), and C_{E1} and O_{2c} (red).

- (oxa)metallacycle species S_1IM-W_{5c} from ethene cycloaddition on adsorption sites C_{A1} and W_{5c}

The S_1 represents Stage 1 as mentioned above, TS denotes transition state, and IM denotes intermediate.

Table 2 again gives the bond lengths upon formation of the C_4 (oxa)metallacycle. Most of the (oxa)metallacycle pathways significantly activate the C═C bond of ethene, except for the S_1IM-O_{2c} (oxa)metallacycle species. We note that for the S_1IM-W_{5c} (oxa)metallacycle species, the $C_{A1}-C_{E2}-C_{E1}$ bond is nearly linear, with a C−C−C angle of 163.1°.

In order to proceed to propagation, the intermediate C_4 (oxa)metallacycle species must be decomposed by cycloreversion to yield a propene molecule; thus, only a methylene compound remains on the surface. Because we have three different (oxa)metallacycle intermediates, S_1IM-W_{6c}, S_1IM-O_{2c}, and S_1IM-W_{5c}, there exist three possible paths to the product in Stage 1. We used the CI-NEB method, with transition states between the three initial adsorption configurations and three C_4 (oxa)metallacycle intermediates, and between the C_4 (oxa)metallacycle intermediates and W═CH_2 + propene, to map out stationary points along the minimum energy paths. Three transition states, $S_1TS_1-W_{6c}$, $S_1TS_1-O_{2c}$, and $S_1TS_1-W_{5c}$, in the cycloaddition step, and three transition states, $S_1TS_2-W_{6c}$, $S_1TS_2-O_{2c}$, and $S_1TS_2-W_{5c}$, in the cycloreversion step, were identified as corresponding to the closing and opening of a four-, five-, or six-membered (oxa)metallacycle ring.

The energy diagram depicting the ethene propagation stage on WO_3 (001) with W═$CHCH_3$ active sites is presented in Figure 5, with specific energies of adsorption and energies of reaction in Table 3. We normalized the total energy of ethene, 2-butene, and clean WO_3 (001) with W═$CHCH_3$ active sites to zero. We denoted adsorption configurations (S_1IN-W_{6c}, S_1IN-O_{2c} and S_1IN-W_{5c}) as W═$CHCH_3$−ethene(ad). For the C_{A1} and O_{2c} binding pathway, the formation of the five-membered (oxa)metallacycle species S_1IM-O_{2c} has the highest activation barrier and the most endothermic reaction energy. However, for the C_{A1} and W_{5c} binding pathway, the decomposition of the six-membered (oxa)metallacycle species S_1IM-W_{5c}, has the highest activation energy barrier. When comparing all energy barriers in ethene propagation, it is easily seen that the C_{A1} and W_{6c} binding pathway, with the four-membered (oxa)metallacycle intermediate, has the lowest activation energy barriers in both the [2 + 2] cycloaddition step and the cycloreversion step. It indicates the small (oxa)metallacycle ring is more active, with stronger electron interaction. This favorable activation energy barrier for C_{A1} and W_{6c} interaction should be sufficient to overcome a small penalty (1.1 kJ/mol) for the overall energy of formation compared to the C_{A1} and W_{5c} interaction. Therefore, ethene preferentially forms a four-membered C_4 (oxa)metallacycle intermediate by [2 + 2] cycloaddition at C_{A1} and W_{6c}, then proceeds to cycloreversion to produce another W═CH_2 active site for further propagation.

Table 3. Calculated Energies of Activation and Energies of Reaction for (Oxa)Metallacycle Formation and Cycloreversion Steps during Ethene Propagation

	formation		cycloreversion	
adsorption configuration	E_a (kJ/mol)	ΔE_{rxn} (kJ/mol)	E_a (kJ/mol)	ΔE_{rxn} (kJ/mol)
(A): S_1IN-W_{6c}	+43.6	+23.8	+71.3	+55.1
(B): S_1IN-O_{2c}	+91.2	+49.8	+81.3	+26.9
(C): S_1IN-W_{5c}	+61.6	+37.6	+119.2	+42.5

The detailed structures of the reaction species involved in the C_{A1} and W_{6c} (A)-type pathway, including transition states, are shown in Figure 6, with bond lengths listed in Table 2. We can see the length of the $W_{6c}-C_{A1}$ and $C_{E1}-C_{E2}$ bonds increase along the propagation pathway, while the distances between C_{A1} and C_{E2}, and between W_{6c} and C_{E1}, decrease. For the transition state $S_1TS_1-W_{6c}$, the $C_{A1}-C_{A2}$ bond is still almost in vertical orientation, although it tilts slightly relative to the surface normal, while the $W_{6c}-C_{E1}$ bond is formed with a length of 2.150 Å. The resulting four-membered ring has a W−C−C−C dihedral angle of 142.7°. For the transition state

dx.doi.org/10.1021/cs500531b | ACS Catal. 2015, 5, 59−72

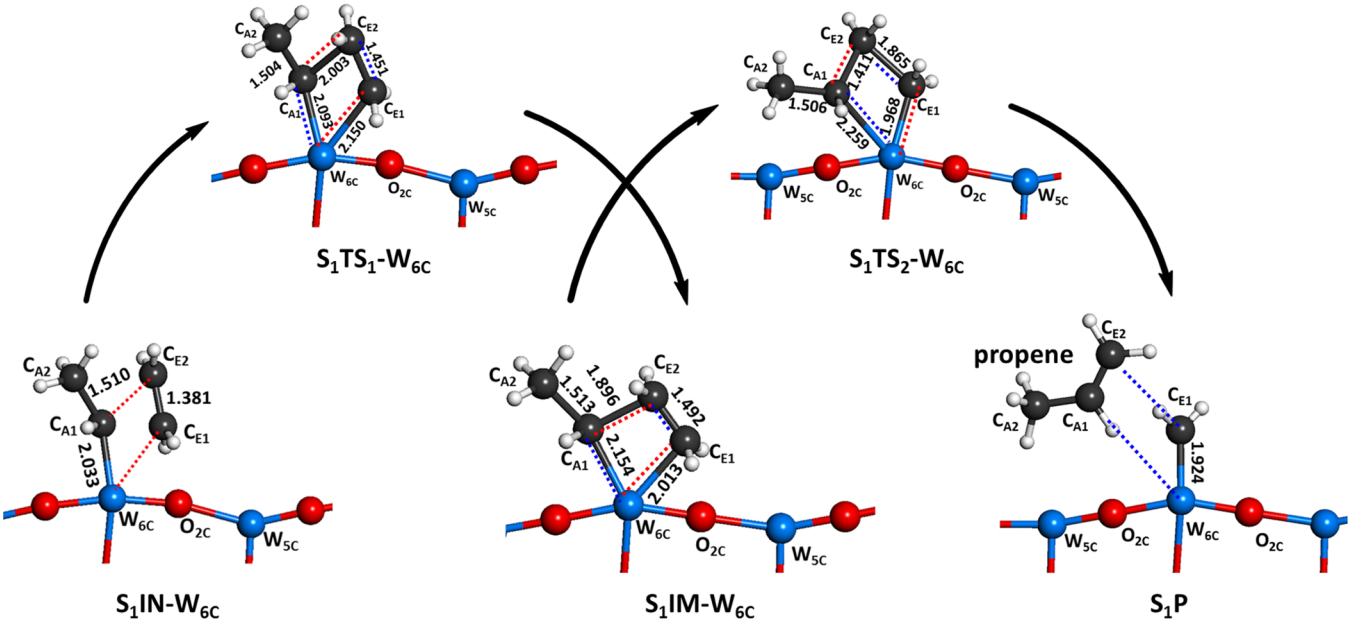

Figure 6. Optimized structures of the initial state, transition states, intermediate, and product along the minimum energy pathway for ethene propagation. The red dashed line denotes the formed bond with decreasing length along the path, and the blue dashed line denotes the broken bond with increasing length along the path.

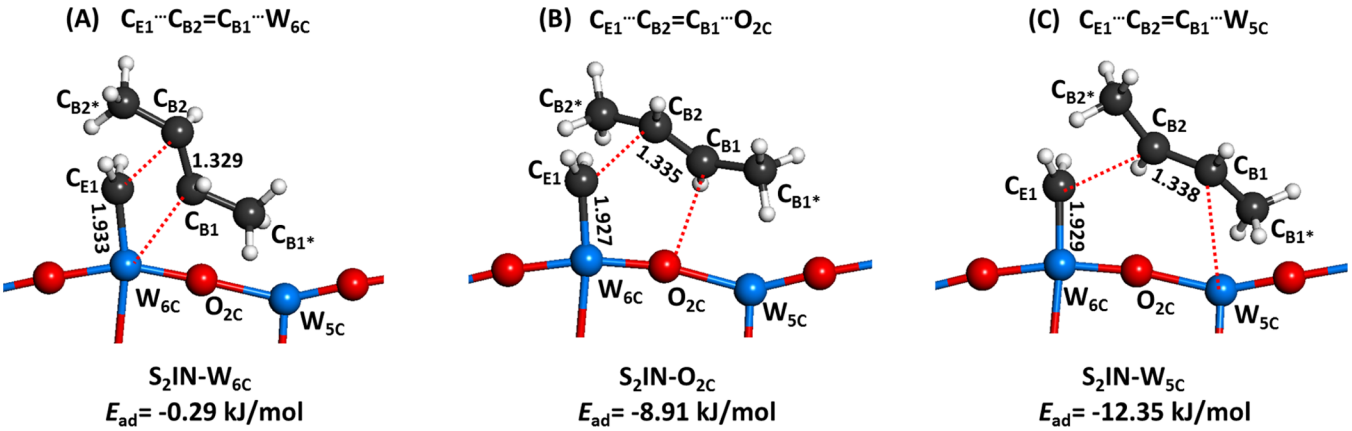

Figure 7. Adsorption configurations and energies for *trans*-2-butene on WO_3 (001) with W=CH_2 active site. C_{B1} and C_{B2} denote two doubly bonded carbons in *trans*-2-butene (secondary carbon atom and tertiary carbon atom in *trans*-2-butene). C_{B1*} and C_{B2*} represent carbon atoms in the nonbinding methyl groups. S_2 denotes Stage 2 of the propagation process, and IN denotes the initial state for propagation.

S_1TS_2–W_{6c}, the W–C–C–C dihedral angle changes to 165.8°, and the bond length of W_{6c}–C_{E1} decreases to 1.968 Å; both are characteristic of the reformation of the W=C bond. The dihedral angle of the intermediate S_1IM–W_{6c} is 149.6°. Thus, the structure of S_1IM–W_{6c} is likened to a puckered ring, rather than a flat four-membered (oxa)metallacycle ring. The methylene compound W=CH_2 (S_1P) is obtained by the breaking of W_{6c}–C_{A1} and C_{E1}–C_{E2} to release one propene molecule. The W=CH_2 now becomes a new W_{6c} active site for propagation in Stage 2.

3.3. Propagation of *trans*-2-Butene for Metathesis.

3.3.1. trans-2-Butene Adsorption on W=CH_2 Active Site. Similar to the study on the ethene propagation stage, we first investigate *trans*-2-butene adsorption on the surface with W=CH_2 active site. The possible two-site adsorption configurations for *trans*-2-butene are

(A) C_{E1}···C_{B2}=C_{B1}···W_{6c}: C_{B1} and C_{B2} adsorb to 6-fold coordinated tungsten W_{6c} and active site carbon C_{E1}, respectively. C_{B1} and C_{B2} denote two doubly bonded carbons (i.e., secondary carbon atom and tertiary carbon atom) in *trans*-2-butene.

(B) C_{E1}···C_{B2}=C_{B1}···O_{2c}: C_{B1} and C_{B2} adsorb to 2-fold coordinated oxygen O_{2c} and active site carbon atom C_{E1}, respectively.

(C) C_{E1}···C_{B2}=C_{B1}···W_{5c}: C_{B1} adsorbs to 5-fold coordinated tungsten W_{5c} while C_{B2} adsorbs to C_{E1}

S_2 denotes Stage 2 of the propagation process.

The optimized structures corresponding to these configurations are shown in Figure 7. For C_{E1}···C_{B2}=C_{B1}···W_{6c} adsorption, corresponding to (A)-type binding, a four-membered ring S_2IN–W_{6c} is formed, which includes four active atoms, W_{6c}, C_{E1},C_{B1}, and C_{B2}. For C_{E1}···C_{B2}=C_{B1}···O_{2c} adsorption, corresponding to (B)-type binding, a five-membered ring S_2IN–O_{2c} is produced, which includes five active atoms W_6c, C_{E1},C_{B1}, C_{B2}, and surface O_{2c}. For C_{E1}···

dx.doi.org/10.1021/cs500531b | ACS Catal. 2015, 5, 59–72

C_{B2}═C_{B1}···W_{5c} adsorption, corresponding to (C)-type binding, the six-membered (oxa)metallacycle ring S_2IN-W_{5c} is formed.

As shown in Figure 7 and Table 1, the strongest adsorption configuration corresponds to the (C)-type binding configuration, with the (B)-type binding configuration being slightly less favored and the (A)-type binding configuration resulting in essentially zero adsorption. This last result can be explained by steric hindrance between the methyl groups in *trans*-2-butene and the W═CH_2 group. The inactive methyl groups require enough physical space given their electrostatics; thus, they hinder the process of *trans*-2-butene adsorption to the catalyst surface.

Table 4 shows that in the (C)-type binding configuration, the W═C bond at the surface, and C═C bond in the *trans*-2-butene molecule are only slightly elongated relative to their values prior to adsorption. Thus, we confirm that *trans*-2-butene adsorption on W═CH_2 is weaker than ethene adsorption on W═$CHCH_3$. The steric effect produced by inactive methyl groups in *trans*-2-butene not only destabilizes the adsorbate, but even hinders bond activation in *trans*-2-butene. Thus, initiating the *trans*-2-butene stage of propagation may be the rate-limiting step of the reaction pathway.

Table 4. Calculated Changes in Bond Lengths upon *trans*-2-Butene Adsorption at W-Carbene Active Sites, And Formation and Cycloreversion of (Oxa)Metallacycles

adsorption	W═C (Å)	$C_{B1}-C_{B2}$ (Å)
before adsorption	1.903	1.329
(A): S_2IN-W_{6c}	1.933	1.329
(B): S_2IN-O_{2c}	1.927	1.335
(C): S_2IN-W_{5c}	1.929	1.338

formation	W═C (Å)	$C_{B1}-C_{B2}$ (Å)	W−C_{B1} or O−C_{B1} (Å)	$C_{E1}-C_{B2}$ (Å)
S_2IN-O_{2c}	2.005	1.435	1.899	1.532
S_2IN-W_{5c}	1.998	1.517	2.225	1.575

cycloreversion	W═C (Å)
S_2IN-O_{2c}	1.935
S_2IN-W_{5c}	1.935

The experimental findings of Chaemchuen et al.[23] suggested that *trans*-2-butene was the dominant reactant during this olefin metathesis process, and other researchers[72,73] have also supported this finding. However, we note that *cis*-2-butene may also have been detected experimentally as a side product of this reaction. For completeness, we modeled the adsorption of *cis*-2-butene on the W-carbene active site, and we found that the energy of adsorption was a little less (E_{ads} = −12.3 kJ/mol) than that for *trans*-2-butene adsorption. We believe that this difference is due to the steric crowding between the methyl groups, which causes the *cis* stereoisomer to be less stable than the *trans*-stereoisomer. Although we stick to the Hérisson−Chauvin mechanism here, we note that the inclusion of *cis*-2-butene in a full microkinetic model could be the subject of future work.

3.3.2. Formation and Cycloreversion of the C_5 (Oxa)-metallacycle. Adsorbed *trans*-2-butene reacts with W═CH_2 active site to form a C_5 (five carbon atoms in total) (oxa)metallacycle species by [2 + 2] cycloaddition. Because of the weak adsorption of S_2IN-W_{6c}, and difficulty in optimizing the structure of the C_5 (oxa)metallacycle due to steric hindrance, we no longer consider *trans*-2-butene cycloaddition on that site. Based on two remaining types of adsorption configurations, two possible C_5 (oxa)metallacycles can be obtained, as shown in Figure 8:

- (oxa)metallacycle species S_2IM-O_{2c} from *trans*-2-butene cycloaddition on adsorption sites C_{E1} and O_{2c}
- (oxa)metallacycle species S_2IM-W_{5c} from *trans*-2-butene cycloaddition on adsorption sites C_{E1} and W_{5c}

The S_2 represents Stage 2 as mentioned above, TS denotes a transition state, and IM denotes an intermediate.

Table 4 again gives the bond lengths upon formation of the C_5 (oxa)metallacycle. Compared to the elongation of bonds in ethene [2 + 2] cycloaddition, we can conclude there is less electron transfer from *trans*-2-butene to W-carbene than from ethene to W-carbene, and hence, the catalytic activation is lower for this step of the propagation process.

To complete the propagation cycle, the intermediate C_5 (oxa)metallacycle species then is decomposed by cycloreversion to yield the second propene molecule and regenerate the initial W═$CHCH_3$ active site. Because we have two (oxa)metallacycle intermediates, S_2IM-O_{2c} and S_2IM-W_{5c}, there exist two possible paths for *trans*-2-butene propagation. Again, we used the CI-NEB method to map out stationary points along these two pathways. Two transition states, $S_2TS_1-O_{2c}$ and $S_2TS_1-W_{5c}$, in the [2 + 2] cycloaddition step, and two transition states, $S_2TS_2-O_{2c}$ and $S_2TS_2-W_{5c}$, in the cycloreversion step, are identified as corresponding to the closing and opening of the five- and six-membered (oxa)metallacycle rings.

The energy diagram depicting the *trans*-2-butene propagation state on WO_3 (001) with W═CH_2 active sites is presented in Figure 5, with specific energies of adsorption and energies of reaction in Table 5. When comparing all energy barriers in

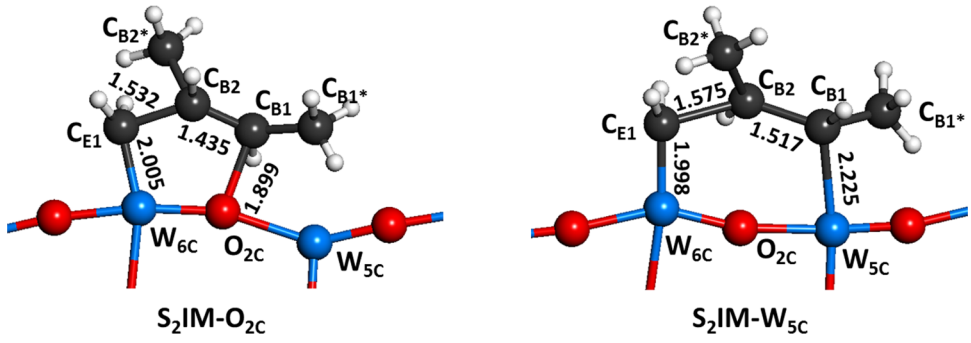

Figure 8. Optimized structures of (oxa)metallacycles from *trans*-2-butene [2 + 2] cycloaddition on WO_3 (001) with W═CH_2 active site. S_2 denotes Stage 2 of the propagation process, and IM denotes the intermediate.

dx.doi.org/10.1021/cs500531b | ACS Catal. 2015, 5, 59−72

Table 5. Calculated Energies of Activation and Energies of Reaction for (Oxa)Metallacycle Formation and Cycloreversion Steps during *trans*-2-Butene Propagation

adsorption configuration	formation		cycloreversion	
	E_a (kJ/mol)	ΔE_{rxn} (kJ/mol)	E_a (kJ/mol)	ΔE_{rxn} (kJ/mol)
(B): S_2IN-O_{2c}	+108.3	+32.7	+46.3	−82.2
(C): S_2IN-W_{5c}	+88.7	+11.6	+17.4	−57.7

trans-2-butene propagation, we find that the C_{E1} and W_{5c} binding pathway, with its six-membered (oxa)metallacycle intermediate, has the lower activation energy barriers in both the [2 + 2] cycloaddition step and the cycloreversion step. Therefore, in Stage 2, *trans*-2-butene preferentially forms a six-membered C_5 (oxa)metallacycle intermediate by [2 + 2] cycloaddition at C_{E1} and W_{5c}, and then proceeds to cycloreversion to regenerate the initial active site W═$CHCH_3$ and complete the propagation cycle. The overall heat of reaction associated with *trans*-2-butene propagation in this stage is estimated to be ΔH_{rxn} = −28.9 kJ/mol. If we compare the preferred energy pathway in Stage 2 with the pathway in Stage 1, we find the highest energy barrier corresponds to the formation of the six-membered (oxa)-metallacycle species, S_2IM-W_{5c}, for *trans*-2-butene propagation, with the activation energy of E_a = +88.7 kJ/mol; this is 17.4 kJ/mol larger than the corresponding energy barrier for the decomposition of the S_1IM-W_{6c} intermediate in cycloreversion step for ethene propagation. Therefore, the formation of the six-membered (oxa)metallacycle species S_2IM-W_{5c} in Stage 2 appears to be the rate-determining step for the whole propagation cycle.

The detailed structure of the reaction species involved in the C_{E1} and W_{5c} (C)-type pathway, including transition states, are shown in Figure 9, with bond lengths listed in Table 4. Due to the overlap of several atoms in the side view of the $S_2TS_1-W_{5c}$ transition state, we have not explicitly labeled the bond lengths; however, we observe similar changes in bond lengths in Stages 1 and 2. Compared to the twisted structure of $S_2TS_1-W_{5c}$, the $S_2TS_2-W_{5c}$ transition state consists of a nearly flat (oxa)-metallacycle, with a dihedral angle of 166.8°. We can see that the initial reactant, trans-2-butene, for Stage 2 of the propagation cycle, isomerizes to the cis-2-butene structure during the [2 + 2] cycloaddition step. This structural conversion can greatly reduce surface strain on the inactive methyl groups and stabilize the six-membered C_5 (oxa)-metallacycle intermediate. However, it also leads to artificially higher energies of activation for the "elementary step", as shown in Figure 5. The second propene product is obtained by breaking the previously elongated $W_{6c}-C_{E1}$ and $C_{B1}-C_{B2}$ bonds. This completes the propagation cycle by regenerating the W═$CHCH_3$ active site for Stage 1 of propagation. We notice, however, that the W═$CHCH_3$ active site regeneration, while structurally similar due to periodic boundary conditions, is not at the same surface W atom. In fact, the cycloreversion produces the W═$CHCH_3$ species at an originally labeled W_{5c} site, instead of at an originally labeled W_{6c} site site. This 5-fold coordinated W_{5c} thus becomes a new 6-fold coordinated tungsten W_{6c} site, due to the formation of $W_{5c}-C_{B2}$. We show this difference using "*" in S_{1P} (Figure 9). This active site migration may explain the low deactivation of the WO_3 catalyst and its high activity for metathesis of ethene and *trans*-2-butene.

3.4. Rate Constants for Propagation Cycle. On the basis of the aforementioned potential energy profiles, depicted in Figure 5, for propagation of ethene and *trans*-2-butene on the tungsten trioxide (WO_3) (001) surface, we demonstrated that the activation energy barrier for [2 + 2] cycloaddition of *trans*-2-butene to form the six-membered C_5 (oxa)metallacycle ring is much higher than other elementary steps. For this reason, we hypothesize that this is the rate-limiting step of propagation, and we proceeded to calculate the forward and reverse rate constants for this process. We used the frequencies of the (oxa)metallacycle intermediates and their corresponding transition states to calculate our best predictions for temper-

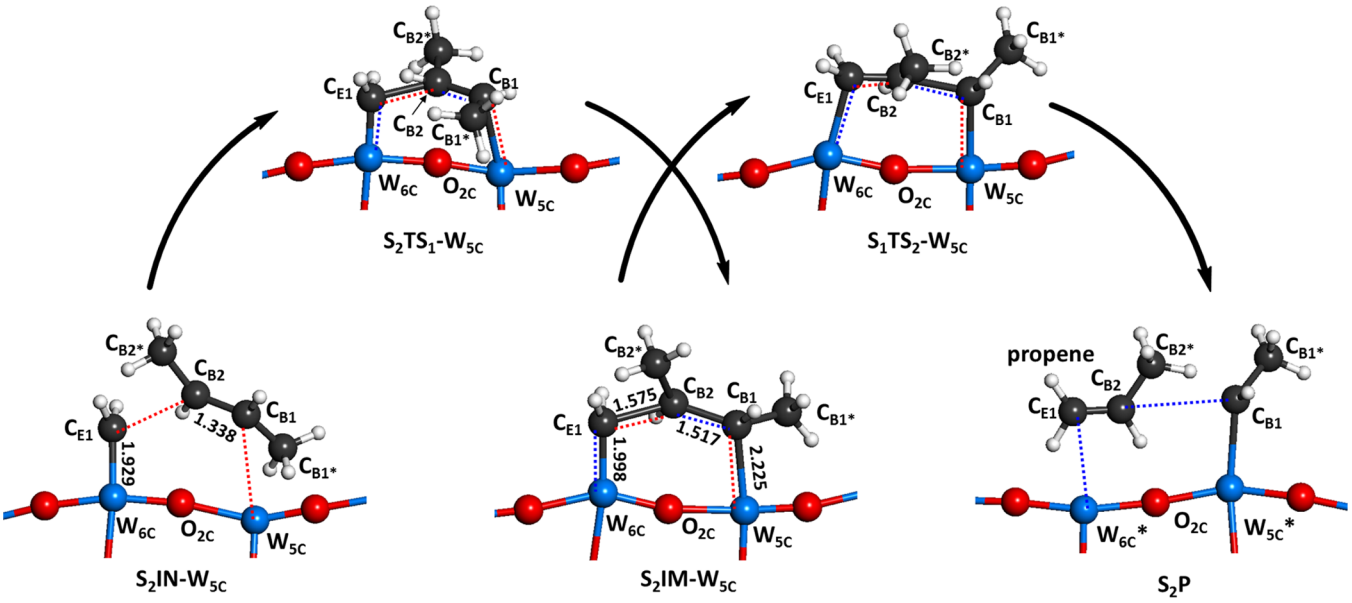

Figure 9. Optimized structures of the initial state, transition states, intermediate and product along the minimum energy pathway for *trans*-2-butene propagation. The red dashed line denotes the formed bond with decreasing length along the path, and the blue dashed line denotes the broken bond with increasing length along the path.

dx.doi.org/10.1021/cs500531b | ACS Catal. 2015, 5, 59−72

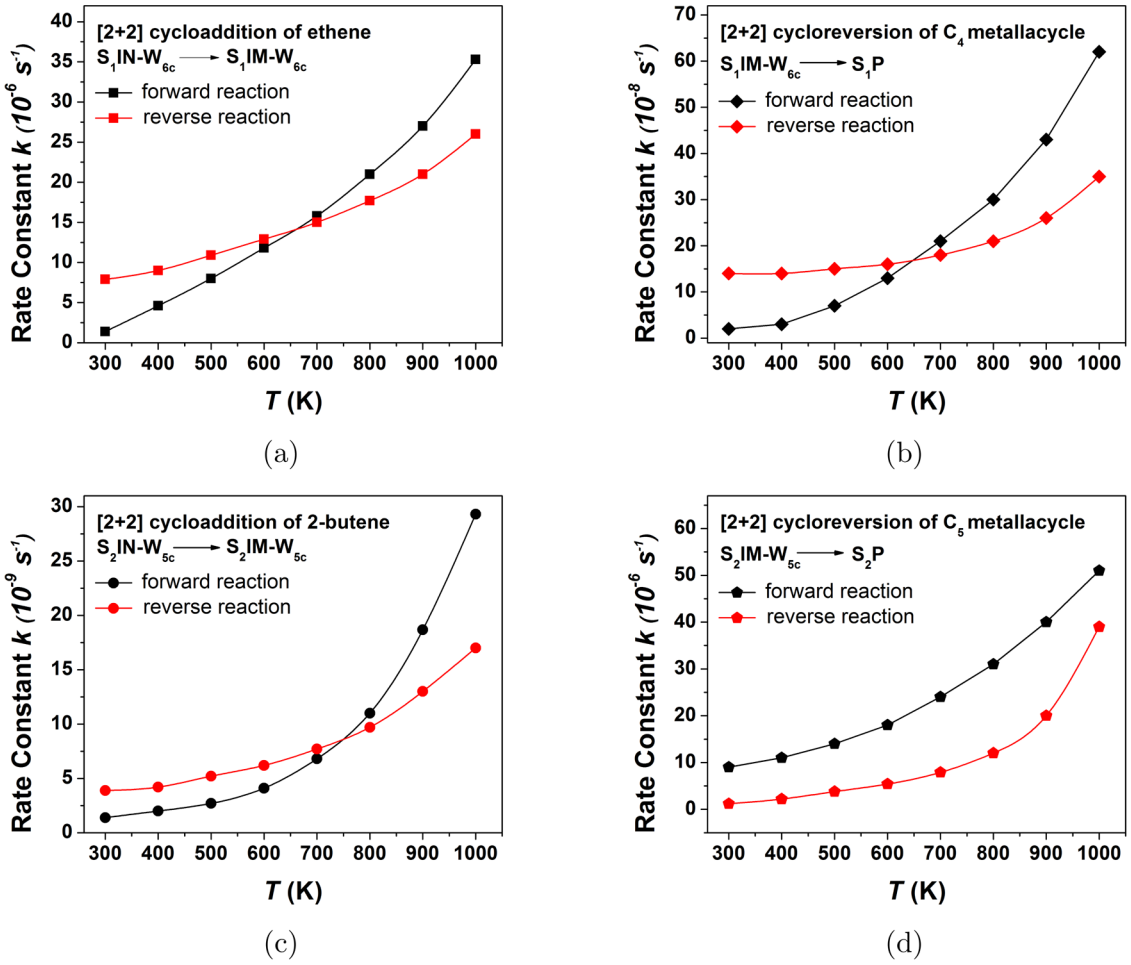

Figure 10. Reaction rate constants, as a function of temperature, of forward and reverse reactions for metathesis propagation. For ethene propagation: (a) formation of C_4 (oxa)metallacycle and (b) cycloreversion of C_4 (oxa)metallacycle. For *trans*-2-butene propagation: (c) formation of C_5 (oxa)metallacycle and (d) cycloreversion of C_5 (oxa)metallacycle.

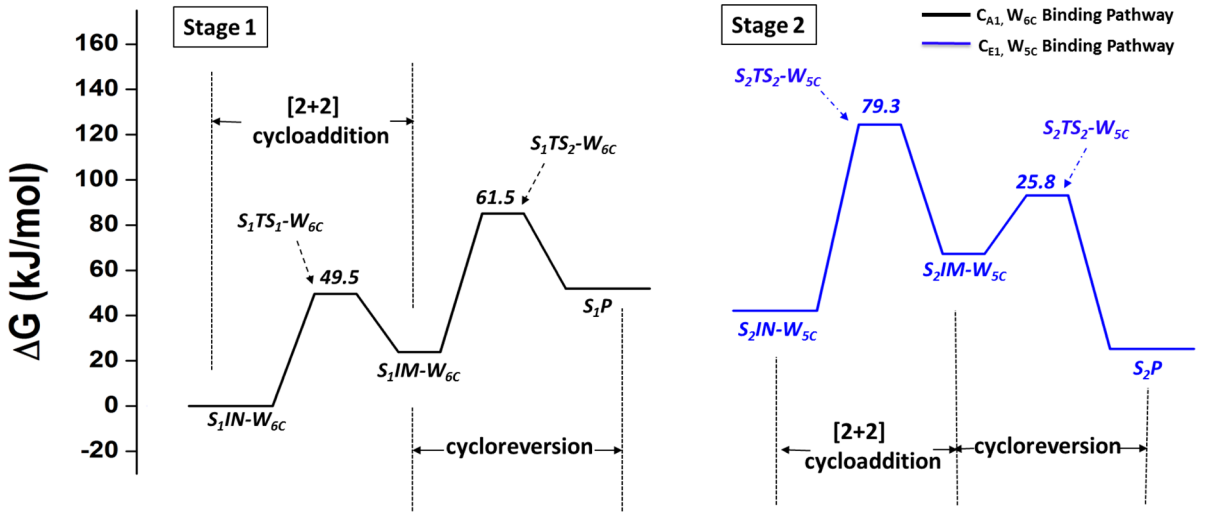

Figure 11. Calculated free energy profile for Stage 1 (black) and Stage 2 (blue) of propagation at 750 K.

ature-dependent rate constants of each forward and reverse step in the two stages of propagation.

As the temperature is increased from 300 to 1000 K, as shown in Figure 10 (panel c), the rate constant of the forward reaction (i.e., [2 + 2] cycloaddition of *trans*-2-butene) increases from k_f (300 K) = 1.39×10^{-9} s^{-1} to k_f (1000 K) = 2.93×10^{-8} s^{-1}, while the rate constant of the reverse reaction increases from k_r (300 K) = 3.89×10^{-9} s^{-1} to k_r (1000K) = 1.71×10^{-8} s^{-1}. When the temperature is below about 750 K, the decomposition rate of the six-membered ring ($S_2IM–W_{5c}$) is

dx.doi.org/10.1021/cs500531b | ACS Catal. 2015, 5, 59–72

faster than the [2 + 2] cycloaddition of *trans*-2-butene. However, the cycloaddition rate constant is more sensitive to temperature, due to its larger activation energy. The cycloaddition thus becomes faster than the decomposition when the temperature is higher than 750 K.

The k vs T relation for stage 1 and the second step of stage 2 also have been plotted as shown in Figures 10 (panels a, b, and d). For [2 + 2] cycloaddition of ethene, the forward reaction rate constant increases almost linearly from k_f (300 K) = 1.57 × 10^{-6} s^{-1} to k_f (1000 K) = 3.73 × 10^{-5} s^{-1}, while the reverse reaction rate constant increases from k_r (300 K) = 7.09 × $10^{-6}s^{-1}$ to k_r (1000 K) = 2.58 × $10^{-5}s^{-1}$. For [2 + 2] cycloreversion of the C_4 (oxa)metallacycle, the forward reaction rate constant increases from k_f (300 K) = 2.12 × 10^{-8} s^{-1} to k_f (1000 K) = 6.43 × 10^{-7} s^{-1}, while the reverse reaction rate constant slowly increases from k_r (300 K) = 1.42 × 10^{-7} s^{-1} to k_r (1000K) = 4.68 × 10^{-7} s^{-1}. For [2 + 2] cycloreversion of C_5 (oxa)metallacycle, the forward reaction rate constant changes from k_f (300 K) = 9.13 × 10^{-6} s^{-1} to k_f (1000 K) = 5.24 × 10^{-5} s^{-1}, while the reverse reaction rate constant increases from k_r (300 K) = 1.33 × $10^{-6}s^{-1}$ to k_r (1000 K) = 3.94 × $10^{-6}s^{-1}$. All of these rate constants are at least an order of magnitude larger than the rate constant of the rate limiting step, which we concluded was the [2 + 2] cycloaddition of *trans*-2-butene; thus, we find good agreement with the results from the energy barriers calculated at 0 K.

We further analyzed the free energy at 750 K. The free energy diagram depicting the stage 1 ethene propagation on WO_3 (001) with W═$CHCH_3$ active sites, and the stage 2 *trans*-2-butene propagation on WO_3 (001) with W═CH_2 active sites, is presented in Figure 11. We normalized the free energy of S_1IN-W_{6c} to zero. Although the free energy of activation of [2 + 2] cycloaddition of *trans*-2-butene at stage 2 displays a lower barrier by 9.4 kJ/mol, compared with the data for the total energy profile at 0 K, the barrier height for the [2 + 2] cycloaddition of *trans*-2-butene is still the largest, which demonstrates again that this is the rate-limiting step.

We note that the activation energy for [2 + 2] cycloreversion of the C_5 (oxa)metallacycle is lower than the activation energy for the reverse reaction of [2 + 2] cycloaddition of *trans*-2-butene, so the propagation can occur even if the temperature falls below 750 K. However, the 750 K threshold is still significant, because if there is an excess of propene product (that has been produced in stage 1), the last step may become slow even it has a low barrier. In this case, the cycloreversion of S_2IM-W_{5c} may hinder the reaction if the temperature is below 750 K. We also concur that there is a possibility of an excess of ethene and *trans*-2-butene if the reaction is carried out far from equilibrium, which would favor cycloaddition. Nevertheless, we suggest 750 K as the lower bound for efficient metathesis of ethene and *trans*-2-butene, and this temperature is corroborated by the 300−500 °C temperature range explored by Chaemchuen et al., and the optimal 90% conversion and 95% selectivity for propene obtained by reaction at 500 °C.[23]

While lateral adsorbate−adsorbate interactions may influence the stability of (oxa)metallacycle intermediates and the kinetics of reaction on the surface with high coverage, we believe that under typical reaction conditions for olefin metathesis, the total surface coverage should be low. Thus, all adsorption energies and activation energies are assumed to be coverage-independent, and reaction rate constants should not be affected much by the surface coverage.

3.5. Conclusions. We have performed a comprehensive density functional theory study of the mechanism for propene production over tungsten trioxide (WO_3) slabs, based on propagation of ethene at W═$CHCH_3$ sites and *trans*-2-butene at W═CH_2 sites. Compared with the mechanism for metathesis on supported Mo catalyst and Re catalysts, the propagation reaction on WO_3 involves two W sites—one 6-fold coordinated, and the other 5-fold coordinated. Because these two active sites are very close (≈ 5 Å) to each other, an alkene double bond will interact with these sites to form stable intermediates, based on the presence of electrophilic and steric effects. We showed that ethene propagation occurs by [2 + 2] cycloaddition at the C_{A1} and W_{6c} sites, followed by cycloreversion of the C_4(oxa)metallacycle to produce another W═CH_2 active site for further propagation. We also showed that *trans*-2-butene propagation occurs by [2 + 2] cycloaddition at the C_{E1} and W_{5c} sites, followed by cycloreversion of the C_5(oxa)metallacycle to regenerate the W═$CHCH_3$ active site. Although it may be argued that ethene adsorption at the W_{5c} site is slightly favored energetically compared to the W_{6c} site, the latter possesses much more favorable activation and kinetic pathway for propene production. Furthermore, we showed that the W═CH_2 sites are less active in the propagation process compared to W═$CHCH_3$, such that the rate-limiting step is the [2 + 2] cycloaddition of *trans*-2-butene to form the six-membered C_5 (oxa)metallacycle ring.

We note that our proposed mechanism still involves the metallacyclobutane intermediate S_1IM-W_{6c}, which is formed by [2 + 2] cycloaddition of the ethene double bond to 6-fold coordinated W alkylidene, and the metallacyclobutane intermediate S_2IM-W_{5c}, which is obtained by [2 + 2] cycloaddition of the 2-butene double bond to 5-fold coordinated W alkylidene. Therefore, our proposed mechanism validates the classical Hérisson and Chauvin metathesis mechanism, while providing detailed structures and energetic information for the intermediates and transition states; this in turn helps us better understand the classical mechanism and the performance of transition metal oxide catalysts in metathesis.

When the temperature is below 750 K, the decomposition rate of the six-membered ring S_2IM-W_{5c} is faster than the [2 + 2] cycloaddition of *trans*-2-butene. However, the cycloaddition rate constant is more sensitive to temperature due to its larger activation energy. The cycloaddition becomes faster than the decomposition when temperature is over 750 K, which we suggest as the lower bound for the reaction temperature by which successful metathesis of ethene and *trans*-2-butene to produce propene may be achieved. We assert that these results lay the foundation for future studies on the kinetics of initiation and propagation, including the role of the catalyst support on the adoption of tetrahedrally versus distorted octahedrally coordinated W in the metal-carbene active site, and the effect of the *cis*-2-butene side product on the reaction mechanism; this will guide the development of more active and selective catalysts for propene production.

■ ASSOCIATED CONTENT

Supporting Information

The following file is available free of charge on the ACS Publications website at DOI: 10.1021/cs500531b.

Additional computational details on the atomic structures and rate constant calculations (PDF)

dx.doi.org/10.1021/cs500531b | *ACS Catal.* 2015, 5, 59−72

AUTHOR INFORMATION

Corresponding Author

*E-mail: clo@wustl.edu.

Notes

The authors declare no competing financial interest.

ACKNOWLEDGMENTS

The authors thank the Center of Excellence on Catalysis and Catalytic Reaction Engineering at Chulalongkorn University in Thailand, particularly the groups of Suphot Phatanasri and Piyasan Praserthdam, for helpful advice and guidance on understanding the experimental basis for olefin metathesis on oxide catalysts. This work used the Extreme Science and Engineering Discovery Environment (XSEDE), which is supported by National Science Foundation grant no. OCI-1053575.

REFERENCES

(1) Oikawa, H.; Shibata, Y.; Inazu, K.; Iwase, Y.; Murai, K.; Hyodo, S.; Kobayashi, G.; Baba, T. *Appl. Catal., A* **2006**, *312*, 181−185.
(2) Spronk, R.; Vanveen, J. A. R.; Mol, J. C. *J. Catal.* **1993**, *144*, 472−483.
(3) Mol, J. C. *Catal. Today* **1999**, *51*, 289−299.
(4) Inaki, Y.; Yoshida, H.; Kimura, K.; Inagaki, S.; Fukushima, Y.; Hattori, T. *Phys. Chem. Chem. Phys.* **2000**, *2*, 5293−5297.
(5) Mitra, B.; Gao, X.; Wachs, I. E.; Hirt, A. M.; Deo, G. *Phys. Chem. Chem. Phys.* **2001**, *3*, 1144−1152.
(6) Mol, J. C. *J. Mol. Catal. A-Chem.* **2004**, *213*, 39−45.
(7) Grubbs, R. H. *Angew. Chem., Int. Ed.* **2006**, *45*, 3760−3765.
(8) Keim, W. *Angew. Chem., Int. Ed.* **2013**, *52*, 12492−12496.
(9) Weissermel, K.; Arpe, H.-J. *Industrial organic chemistry*, 3rd ed.; VCH: Weinheim, 1997.
(10) Tsuji, J. *Transition Metal Reagents and Catalysts*; John Wiley & Sons, Ltd: Chichester, U.K., 2003.
(11) Handzlik, J. *J. Mol. Catal. A-Chem.* **2010**, *316*, 106−111.
(12) Luo, G.; Luo, Y.; Maeda, S.; Qu, J.; Hou, Z.; Ohno, K. *Organometallics* **2014**, *33*, 3840−3846.
(13) Banks, R.*Catalysis*; Topics in Current Chemistry; Springer: Berlin/Heidelberg, 1972; Vol. *25*; pp 39−69.
(14) Thomas, R.; van Oers, E. M.; de Beer, V. H. J.; Moulijn, J. A. *J. Catal.* **1983**, *84*, 275−287.
(15) K. Ivin, J. M. *Olefin Metathesis and Metathesis Polymerization*; Academic Press: San Diego, 1997.
(16) Chen, S.-L.; Wang, Y.; Yuan, G.; Hua, D.; Zheng, M.; Zhang, J. *Chem. Eng. Technol.* **2013**, *36*, 795−800.
(17) Davazoglou, D.; Moutsakis, A.; Valamontes, V.; Psycharis, V.; Tsamakis, D. *J. Electrochem. Soc.* **1997**, *144*, 595−599.
(18) Huang, S.; Liu, S.; Xin, W.; Bai, J.; Xie, S.; Wang, Q.; Xu, L. *J. Mol. Catal. A-Chem.* **2005**, *226*, 61−68.
(19) Huang, S.; Liu, S.; Zhu, Q.; Zhu, X.; Xin, W.; Liu, H.; Feng, Z.; Li, C.; Xie, S.; Wang, Q.; Xu, L. *Appl. Catal., A* **2007**, *323*, 94−103.
(20) Thomas, R.; Kerkhof, F.; Moulijn, J.; Medema, J.; de Beer, V. *J. Catal.* **1980**, *61*, 559−561.
(21) Salvati, L.; Makovsky, L. E.; Stencel, J. M.; Brown, F. R.; Hercules, D. M. *J. Phys. Chem.* **1981**, *85*, 3700−3707.
(22) Liu, H.; Huang, S.; Zhang, L.; Liu, S.; Xin, W.; Xu, L. *Catal. Commun.* **2009**, *10*, 544−548.
(23) Chaemchuen, S.; Phatanasri, S.; Verpoort, F.; Sae-ma, N.; Suriye, K. *Kinet. Catal* **2012**, *53*, 247−252.
(24) Jean-Louis Hérisson, P.; Chauvin, Y. *Die Makromol. Chem.* **1971**, *141*, 161−176.
(25) Shelimov, B. N.; Elev, I. V.; Kazansky, V. B. *J. Mol. Catal.* **1988**, *46*, 187−200.
(26) Tarasov, A. L.; Shelimov, B. N.; Kazansky, V. B.; Mol, J. C. *J. Mol. Catal. A-Chem.* **1997**, *115*, 219−228.
(27) Szeto, K. C.; Mazoyer, E.; Merle, N.; Norsic, S.; Basset, J.-M.; Nicholas, C. P.; Taoufik, M. *ACS Catal.* **2013**, *3*, 2162−2168.
(28) Adlhart, C.; Chen, P. *J. Am. Chem. Soc.* **2004**, *126*, 3496−3510.
(29) Grubbs, R. H. *Tetrahedron* **2004**, *60*, 7117−7140.
(30) Schrock, R. R. *J. Mol. Catal. A-Chem.* **2004**, *213*, 21−30.
(31) Handzlik, J.; Sautet, P. *J. Catal.* **2008**, *256*, 1−14.
(32) Adlhart, C.; Chen, P. *Angew. Chem., Int. Ed.* **2002**, *41*, 4484−4487.
(33) Wu, Y.-D.; Peng, Z.-H. *Inorg. Chim. Acta* **2003**, *345*, 241−254.
(34) Goumans, T. P. M.; Ehlers, A. W.; Lammertsma, K. *Organometallics* **2005**, *24*, 3200−3206.
(35) Handzlik, J.; Ogonowski, J.; Tokarz-Sobieraj, R. *Catal. Today* **2005**, *101*, 163−173.
(36) Handzlik, J. *Surf. Sci.* **2007**, *601*, 2054−2065.
(37) Cortright, R.; Dumesic, J. *Advances in Catalysis*; Academic Press: San Diego, California: 2001; Vol. *46*; pp 161 − 264.
(38) Cheng, Z.; Lo, C. S. *ACS Catal.* **2012**, *2*, 341−349.
(39) Jones, F.; Rawlings, K.; Foord, J.; Egdell, R.; Pethica, J.; Wanklyn, B.; Parker, S.; Oliver, P. *Surf. Sci.* **1996**, *359*, 107−121.
(40) Tanner, R.; Altman, E. *J. Vac. Sci. Technol. A* **2001**, *19*, 1502.
(41) Poater, A.; Pump, E.; Vummaleti, S. V. C.; Cavallo, L. *J. Chem. Theory Comput.* **2014**, *10*, 4442−4448.
(42) Solans-Monfort, X.; Copéret, C.; Eisenstein, O. *Organometallics* **2012**, *31*, 6812−6822.
(43) Wang, Y.; Chen, Q.; Yang, W.; Xie, Z.; Xu, W.; Huang, D. *Appl. Catal., A* **2003**, *250*, 25−37.
(44) Huang, S.; Chen, F.; Liu, S.; Zhu, Q.; Zhu, X.; Xin, W.; Feng, Z.; Li, C.; Wang, Q.; Xu, L. *J. Mol. Catal. A-Chem.* **2007**, *267*, 224−233.
(45) Wijs, G. A. d.; Boer, P. K. d.; Groot, R. A. d.; Kresse, G. *Phys. Rev. B* **1999**, *59*, 2684−2693.
(46) Migas, D. B.; Shaposhnikov, V. L.; Rodin, V. N.; Borisenko, V. E. *J. Appl. Phys.* **2010**, *108*, 093713.
(47) Ling, S.; Mei, D.; Gutowski, M. *Catal. Today* **2011**, *165*, 41−48.
(48) Sundberg, M.; Tilley, R. J. D. *J. Solid State Chem.* **1974**, *11*, 150−160.
(49) Salje, E.; Viswanathan, K. *Acta Crystallogr. A* **1975**, *A31*, 356−359.
(50) Tanisaki, S. *J. Phys. Soc. Jpn.* **1960**, *15*, 566−573.
(51) Woodward, P.; Sleight, A.; Vogt, T. *J. Solid State Chem.* **1997**, *131*, 9−17.
(52) Roussel, P.; Labbé, P.; Leligny, H.; Groult, D.; Foury-Leylekian, P.; Pouget, J. P. *Phys. Rev. B* **2000**, *62*, 176−188.
(53) Dixon, R.; Williams, J.; Morris, D.; Rebane, J.; Jones, F.; Egdell, R.; Downes, S. *Surf. Sci.* **1998**, *399*, 199−211.
(54) Tanner, R. E.; Meethunkij, P.; Altman, E. I. *J. Phys. Chem. B* **2000**, *104*, 12315−12323.
(55) Tanner, R. E.; Altman, E. I. *J. Vac. Sci. Technol. A* **2001**, *19*, 1502−1509.
(56) Ma, S.; Frederick, B. G. *J. Phys. Chem. B* **2003**, *107*, 11960−11969.
(57) Kresse, G.; Hafner, J. *Phys. Rev. B* **1993**, *47*, 558−561.
(58) Kresse, G.; Furthmüller, J. *Comput. Mater. Sci.* **1996**, *6*, 15−50.
(59) Kresse, G.; Furthmüller, J. *Phys. Rev. B* **1996**, *54*, 11169−11186.
(60) Perdew, J. P.; Burke, K.; Ernzerhof, M. *Phys. Rev. Lett.* **1996**, *77*, 3865−3868.
(61) Blöchl, P. E. *Phys. Rev. B* **1994**, *50*, 17953−17979.
(62) Kresse, G.; Joubert, D. *Phys. Rev. B* **1999**, *59*, 1758.
(63) Blöchl, P. E.; Jepsen, O.; Andersen, O. K. *Phys. Rev. B* **1994**, *49*, 16223−16233.
(64) Yakovkin, I.; Gutowski, M. *Surf. Sci.* **2007**, *601*, 1481−1488.
(65) Grimme, S. *J. Comput. Chem.* **2006**, *27*, 1787−1799.
(66) Jónsson, H.; Mills, G.; Jacobsen, K. W. In *Classical and Quantum Dynamics in Condensed Phase Simulations*; Berne, B. J., Ciccotti, G., Coker, D. F., Eds.; World Scientific: Singapore, 1998; pp 385−404.
(67) Henkelman, G.; Uberuaga, B. P.; Jonsson, H. *J. Chem. Phys.* **2000**, *113*, 9901−9904.
(68) Yaws, C. L.*The Yaws handbook of thermodynamic properties for hydrocarbons and chemicals*; Gulf Publishing Company: Houston, Texas, 2006.
(69) Logadottir, A.; Rod, T.; Nørskov, J.; Hammer, B.; Dahl, S.; Jacobsen, C. *J. Catal.* **2001**, *197*, 229−231.

(70) Norskov, J.; Bligaard, T.; Logadottir, A.; Bahn, S.; Hansen, L.; Bollinger, M.; Bengaard, H.; Hammer, B.; Sljivancanin, Z.; Mavrikakis, M.; Xu, Y.; Dahl, S.; Jacobsen, C. *J. Catal.* **2002**, *209*, 275−278.
(71) Bligaard, T.; Nørskov, J.; Dahl, S.; Matthiesen, J.; Christensen, C.; Sehested, J. *J. Catal.* **2004**, *224*, 206−217.
(72) Mazoyer, E.; Szeto, K. C.; Merle, N.; Norsic, S.; Boyron, O.; Basset, J.-M.; Taoufik, M.; Nicholas, C. P. *J. Catal.* **2013**, *301*, 1−7.
(73) Debecker, D. P.; Stoyanova, M.; Rodemerck, U.; Colbeau-Justin, F.; Boissère, C.; Chaumonnot, A.; Bonduelle, A.; Sanchez, C. *Appl. Catal., A* **2014**, *470*, 458−466.